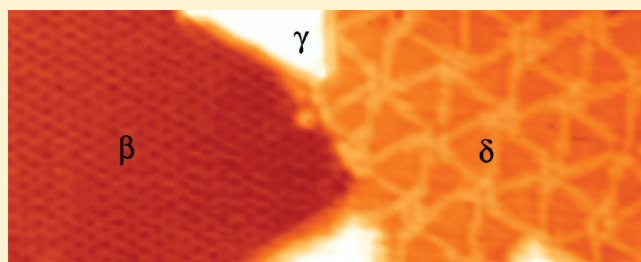# Surface Structures of Ultrathin TiO$_x$ Films on Au(111)

Chen Wu,*,[†] Matthew S. J. Marshall,[‡,†] and Martin R. Castell*,[†]

[†]Department of Materials, University of Oxford, Parks Road, Oxford, OX1 3PH, United Kingdom

ABSTRACT: Ultrathin films of titanium oxide were grown on $(22 \times \sqrt{3})$-reconstructed Au(111) surfaces by Ti evaporation in ultrahigh vacuum (UHV). Following Ti deposition onto room temperature Au substrates, the samples were oxidized at 600 °C in 10^{-6} Pa O$_2$. Scanning tunneling microscopy (STM) images show that three different ordered TiO$_x$ film structures form as the amount of deposited Ti is increased. Auger electron spectroscopy (AES) was used to measure the stoichiometry of the films. The first structure occurs for Ti surface coverages of <0.5 monolayer (ML), and exhibits a (2×2) reconstruction that has

hexagonal symmetry and is termed the honeycomb structure. This (2×2) structure has Ti$_2$O$_3$ stoichiometry. The second structure arises after depositing 0.5 ML - 1.8 MLs of Ti and resembles a pinwheel shape. The pinwheel structure forms a $(\sqrt{67} \times \sqrt{67})R12.2°$ Moiré pattern, and it tends to coexist with the (2×2) reconstruction. The third structure occurs for >0.5 ML Ti depositions and forms triangular shaped islands with a measured stoichiometry of TiO$_{1.3}$. Further increasing the amount of deposited Ti causes film growth to continue via the coalescence of the triangular islands. Atomic models are proposed for the honeycomb and pinwheel structures.

INTRODUCTION

Titanium oxide is a technologically important material in applications ranging from catalysis[1-4] to gas sensing[5-7] and solar energy conversion.[8-10] These applications have stimulated numerous studies on the surface science of rutile and anatase, which are the two most common TiO$_2$ polymorphs. Ultrathin films of TiO$_x$ have different structures and properties than bulk crystal terminations, with the result that an increasing interest is developing in this field. TiO$_x$ thin films have been grown on metal substrates including Ru(0001),[11] Ni(110),[12-14] Pt(001),[21,22] Mo(112),[23-24] and Cu (001).[25-26] Variations in film stoichiometry and the epitaxial nature of growth influence the structure of the films, as observed on TiO$_x$/Pt(111).[15-20] Thin film growth of TiO$_x$ on Pt[27,28] is a model system for studying the strong metal support interaction (SMSI). This phenomenon is important in the study of oxide supported noble metal catalysts.[29] Similarly, growing TiO$_x$ on Au substrates is partially motivated by the discovery of the catalytic properties of TiO$_2$ supported Au nanoclusters.[30,31] There are no reported studies of epitaxial thin films of TiO$_x$ on Au to date. However, Osgood et al. used three methods to synthesize TiO$_2$ nanocrystals on Au(111): room temperature deposition of Ti on Au(111) in O$_2$ followed by postannealing,[32] reactive-layer-assisted deposition,[33,34] and annealing a Ti−Au surface alloy on a Au(111) substrate in oxygen.[35]

In this work, we report a study where Ti was deposited onto reconstructed Au(111) room temperature substrates, and subsequently oxidized in O$_2$ at 600 °C. This method produced three different epitaxial structures depending on the amount of Ti deposited. The first structure resembles a hexagonal honeycomb pattern, while the second exhibits a pinwheel shape. Both structures wet the substrate surface and form the first monolayer (ML).

From the second ML onward, film growth proceeds via the coalescence of triangular islands. The structures are characterized using scanning tunneling microscopy (STM) and Auger electron spectroscopy (AES). Atomic models are proposed based on the STM and Auger data in combination with results from previous related studies.[15,17,36-39]

EXPERIMENTAL SECTION

Mica-supported Au(111) single crystals (Agilent Technologies, U. K.) were used as the substrates for TiO$_x$ thin film growth. To form clean reconstructed substrate surfaces, the Au(111) samples were Ar$^+$ ion sputtered for 10 min with an ion flux of 86 μA/cm^2, followed by annealing in UHV at approximately 600 °C for 1.5 h. The resulting $(22 \times \sqrt{3})$ reconstruction on the Au(111) surfaces was confirmed by STM prior to the deposition of Ti. Ti was deposited onto the gold substrates in UHV from an electron beam evaporator (Oxford Applied Research EGN4) using 99.99% pure Ti rods (Johnson Matthey plc, U. K.). The samples were then annealed in 10^{-6} Pa O$_2$ at ~600 °C for 30 min to form oxidized thin films. The partial pressure of O$_2$ was kept constant for 30 min during the sample cooling period following annealing. The amount of deposited Ti is estimated in monolayer equivalents, which correspond to the density of Au atoms per unit area of (1×1)-Au(111) $(1.4 \times 10^{15}$ atoms per cm^2).

STM imaging was carried out in two separate JEOL UHV-STM systems, a JSTM4500XT and a JSTM4500S, both operating at base pressures of 10^{-8} Pa. Imaging was performed in

constant current mode (unless otherwise stated) using electrochemically etched W tips with the bias voltage applied to the sample. STM images were processed with WSxM[40] and FabViewer[41] software. Attached to the JSTM4500S is a UHV chamber containing a JEOL TM Z9043T scanning electron microscope (SEM). The SEM chamber also contains a SPECS PHOIBOS 100 hemispherical energy analyzer, used to measure the energy of the Auger electrons. The focused electron beam of the SEM serves as the excitation source for Auger electron generation, allowing AES to be performed from small regions. The signal-to-noise ratio of the Auger spectroscopy setup is sufficiently high that quantitative peak height analysis can be performed from undifferentiated spectra.

■ RESULTS

Scanning Tunneling Microscopy. The STM images in Figure 1 show the evolution of ultrathin TiO_x films on Au(111) with increasing Ti coverage. We observe three types of TiO_x structures that form as the surface coverage is increased. The three structures are designated as honeycomb, pinwheel, and triangular islands in accordance with their appearance in the STM images. Different structures are marked as α (reconstructed Au), β (honeycomb TiO_x), γ (triangular island TiO_x), and δ (pinwheel TiO_x) in the STM images containing multiple structures.
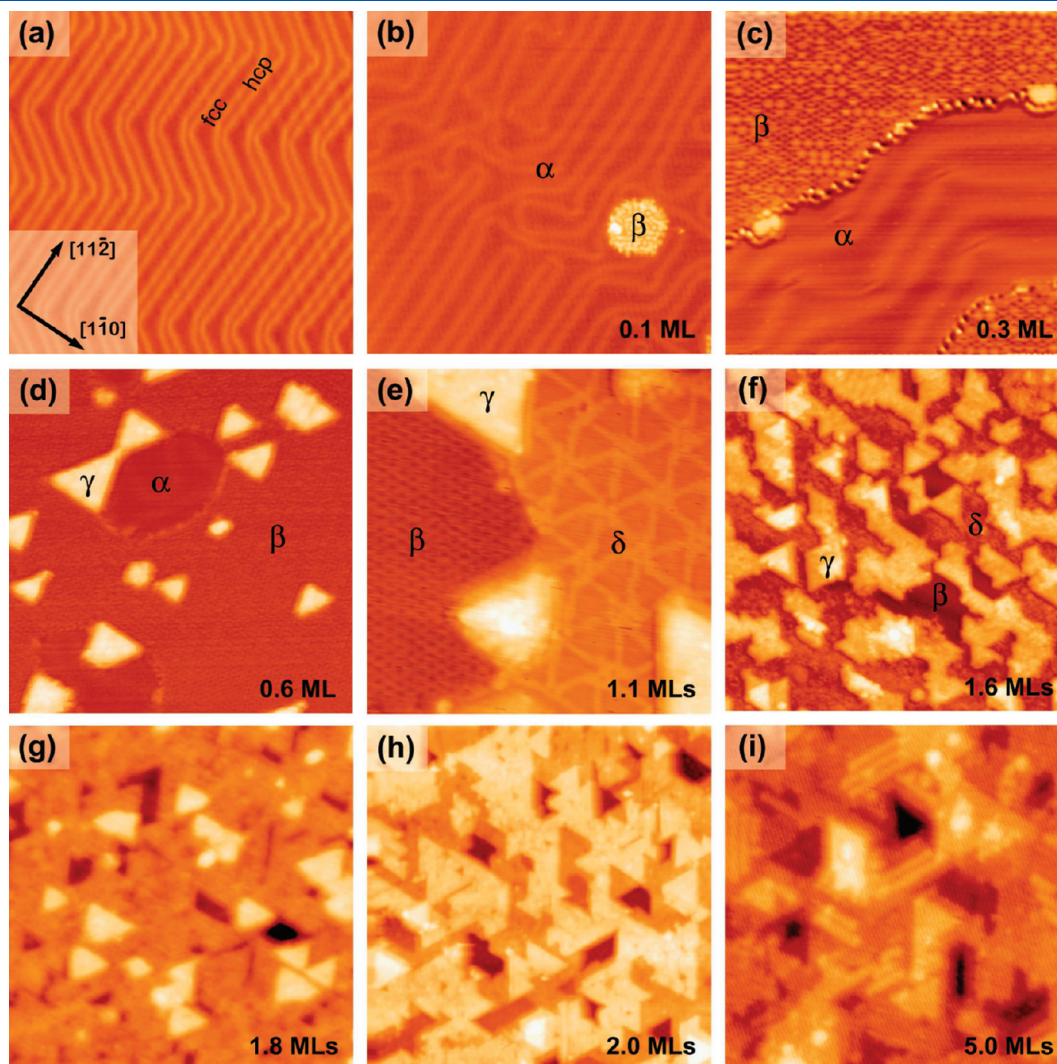

Figure 1. Increasing amounts of Ti were deposited at room temperature onto reconstructed Au(111) surfaces, followed by annealing at 600 °C in 10^{-6} Pa of O_2 for 30 min. The Ti deposition amounts are marked on the STM images. Different structures are labeled as α (reconstructed Au), β (honeycomb (2×2) TiO_x), γ (triangular island TiO_x), and δ (pinwheel TiO_x) in the STM images with multiple structures. (a) $(22 \times \sqrt{3})$-reconstructed Au(111) substrate (Image size: 75×75 nm^2, $V_s = -1.85$ V, $I_t = 0.20$ nA). (b) 0.1 ML: a small bright island of the honeycomb structure (Image size: 59×59 nm^2, $V_s = 1.30$ V, $I_t = 0.20$ nA). (c) 0.3 ML: larger coverage of honeycomb structure (Image size: 32×32 nm^2, $V_s = 0.32$ V, $I_t = 0.22$ nA). (d) 0.6 ML: honeycomb structure and triangular islands on the reconstructed Au surface (Image size: 31×31 nm^2, $V_s = 1.00$ V, $I_t = 0.20$ nA). (e) 1.1 MLs: coexisting honeycomb structure, pinwheel structure and triangular islands (Image size: 18×18 nm^2, $V_s = 0.92$ V, $I_t = 0.20$ nA). (f) 1.6 MLs: a surface almost fully covered by pinwheels with small areas of honeycomb in between and triangular islands on top (Image size: 55×55 nm^2, $V_s = 1.39$ V, $I_t = 0.20$ nA). (g) 1.8 MLs: an almost completed layer of triangular islands with several islands on top (Image size: 37×37 nm^2, $V_s = 0.98$ V, $I_t = 0.22$ nA). (h) 2.0 MLs: several TiO_x layers form with characteristic triangular shape after additional UHV annealing at 600 °C for 3.5 h (Image size: 50×50 nm^2, $V_s = 0.65$ V, $I_t = 0.20$ nA). (i) 5.0 MLs: row structures appear on the triangular islands with subsequent UHV annealing at 600 °C for 1.5 h (Image size: 27×27 nm^2, $V_s = 1.14$ V, $I_t = 0.20$ nA).
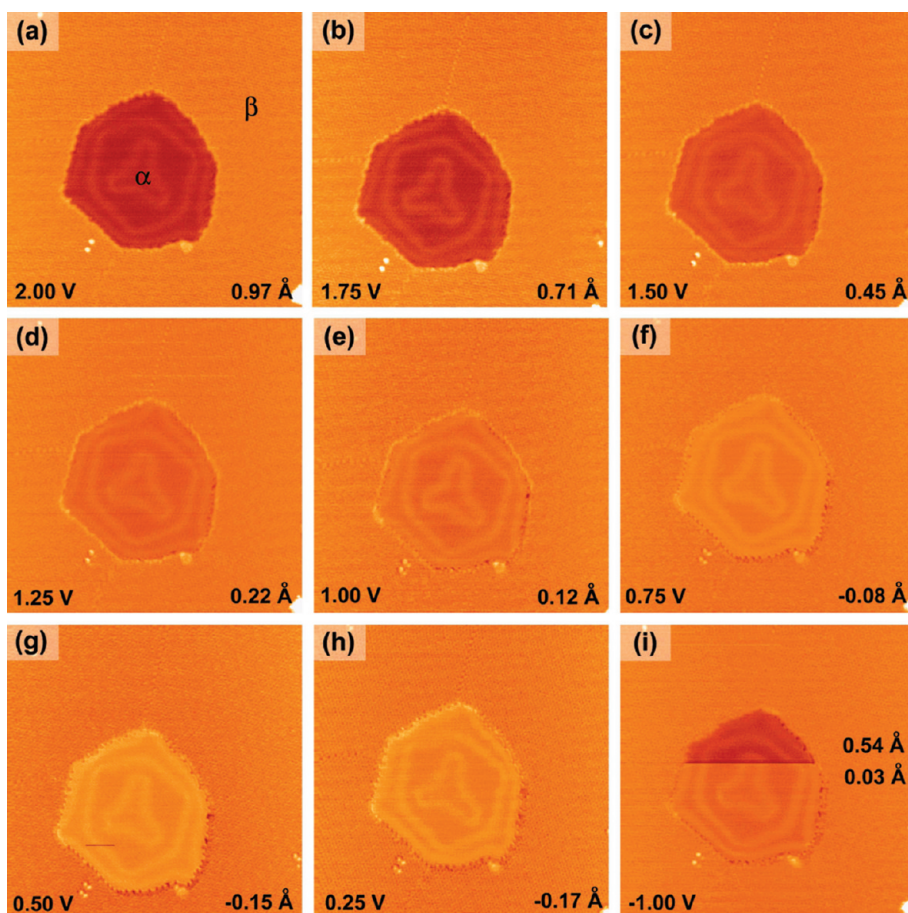
Figure 2. STM images showing the bias and tip dependent apparent height of the honeycomb TiO_x structure (β) relative to the Au(111) substrate (α). The images were taken from the same area with different voltages applied to the sample. All of the images have the same size (50×50 nm^2) and the same imaging current ($I_t = 0.20$ nA), while the sample bias has been decreased from 2.00 to 0.25 V in steps of 0.25 V for images (a)−(h). In image (i), a change in the relative apparent height of the TiO_x structure can be seen following a tip change half-way through the image. The apparent height of the TiO_x structure on the Au(111) reconstruction is indicated on each image.

Figure 1a shows an STM image of the Au(111) surface. Unreconstructed Au(111) planes consist of hexagonal lattices as Au is a face centered cubic (fcc) crystal. The reconstructed Au(111) surface, however, is seen as a complex structure of paired rows. The bright lines in the STM image are boundaries between unfaulted fcc and faulted hcp stacking.[42] This regular stacking sequence transition produces paired rows that have $(22 \times \sqrt{3})$ unit cells and run along the $\langle 11\overline{2} \rangle$ directions. The surface usually has different domains[43] that exhibit a herringbone pattern as shown in Figure 1a.

Figure 1b is an STM image of a Au(111) surface following the deposition of 0.1 ML of Ti with subsequent oxidation. A small bright TiO_x island can be seen toward the right of the image. The island is surrounded by the familiar double rows of the reconstructed Au(111) surface. The island has a hexagonal honeycomb structure which lifts the gold reconstruction, indicating a significant interaction between the substrate and the TiO_x overlayer. In Figure 1c, an STM image shows a higher surface coverage of the honeycomb structure following 0.3 ML Ti deposition.

With further increased Ti coverage of 0.6 ML, triangular islands arise and coexist with the honeycomb structure on the surface. Some reconstructed Au areas are still visible in Figure 1d. The STM image in Figure 1e shows a surface composed of the honeycomb, pinwheel, and triangular islands following the deposition of 1.1 MLs of Ti. Measuring the heights of the surface

features from the STM image indicates that the pinwheels are approximately 0.1 Å higher than the honeycomb structure. Pinwheel structures were also observed on the bare Au surface with lower Ti deposition amounts. Therefore, the pinwheel structure does not grow on top of the honeycomb structure as may be the appearance in Figure 1e, but rather the pinwheel structure wets the substrate surface to form the first TiO_x layer in a different way from the honeycomb structure.

In Figure 1f, the STM image shows triangular islands growing on top of honeycomb and pinwheel structures following 1.6 MLs Ti deposition. Some areas of the islands appear brighter, indicating that a second layer of islands has started to form before the completion of the first triangular type TiO_x layer. Slightly increasing the deposition amount of Ti to 1.8 MLs leads to an almost completed first layer of triangular islands with several islands on top. The film continues to grow via the coalescence of triangular islands as the deposition amount is increased to 2.0 MLs. Figure 1h shows an STM image of the triangular islands following UHV annealing at 600 °C for 3.5 h. Atomic resolution STM of the triangular islands was not achieved. A 5.0 ML Ti deposition followed by a 1.5 h postoxidation anneal in UHV resulted in the formation of row structures on top of the triangular islands, as shown in Figure 1i. The row structures only appear on thicker films.

Changes in sample bias or the apical atom of the STM tip affect the apparent height of the honeycomb TiO_x structure compared to the Au(111) substrate. This is demonstrated by a series of STM images taken from the same surface area (0.7 ML of Ti coverage) in Figure 2. The images have an area of bare Au substrate (α) in the center surrounded by the honeycomb TiO_x structure (β). Again, the Au reconstruction is lifted by the honeycomb structure and winds itself up in the formation of a triangular-shaped feature at the image center. A decreasing apparent height from 0.97 Å to −0.17 Å of the honeycomb TiO_x structure is observed with a decrease from 2.00 to 0.25 V in sample bias. Although the TiO_x layer is topographically higher than the Au substrate, for sample biases below 0.75 V, the Au reconstruction looks brighter than the TiO_x overlayer (Figure 2f−h). This type of bias dependent height behavior is not unusual,[44,45] and has been demonstrated dramatically for Au monolayer islands on a $SrTiO_3(001)$ substrate.[46] The tunneling current in STM depends on both the tip−sample separation and the local density of states (LDOS) of the sample. By changing sample bias, different parts of the LDOS energy spectrum are accessed, giving rise to different apparent heights in STM images.

Figure 2i shows a contrast change caused by a spontaneous tip change half-way through the image, despite a constant imaging bias being applied. In the upper half of the image, the Au reconstruction appears darker than the surrounding TiO_x honeycomb structure, while in the lower half, the two structures appear to have similar brightness. This is almost certainly due to a change in the tip apex structure. This phenomenon is also often observed[47,48] and it is usually assigned to whether a metal atom or an adsorbate is at the tip apex.

An atomic resolution STM image of the hexagonal honeycomb TiO_x structure is shown in Figure 3a with a unit cell indicated. Arrows marked as "i" and "ii" denote the line profiles shown in Figure 3b,c. A periodicity of 5.9 ± 0.3 Å is measured in Figure 3b along the Au [1$\bar{1}$0] direction. The unit cell is aligned with the crystallographic directions of the gold substrate, and corresponds to a (2 × 2) reconstruction for the epitaxial honeycomb structure on the Au(111) surface. The fcc crystallographic unit cell of Au has dimensions of 4.08 Å, and the close packed [1$\bar{1}$0] direction on the (111) surface has a (1 × 1) periodicity of 2.89 Å. Figure 3c shows the spacing between adjacent bright spots in the image (approximately 3.3 Å) at the edges of the hexagons. The bright spots in the STM image are thought to correspond to the locations of the Ti atoms.[44]

In Figure 4a, an STM image shows coexisting honeycomb, pinwheel, and triangular islands. A pinwheel is outlined in Figure 4a by six interlocking triangles around a central hub. The hubs can be connected to illustrate the unit cells of the pinwheel structure as shown in Figure 4b. The two unit cells in Figure 4b are rotated with respect to each other and demonstrate that multiple domains of pinwheel structure coexist on the surface. The spokes of the pinwheels are brighter in appearance than the areas within the triangles. Since the unit cells of the honeycomb structure form a (2 × 2) reconstruction, which is unrotated with respect to the substrate surface, the honeycomb structure can be used as a reference to determine the crystallographic orientations of the pinwheels. In Figure 4a, the measured angle (θ) between the spoke of the pinwheel and the honeycomb is approximately 2°, while the measured angle (φ) between the unit cells of the pinwheel and the honeycomb structures is approximately 13°. Atomic resolution of the pinwheels (Figure 4c) was achieved using constant height imaging
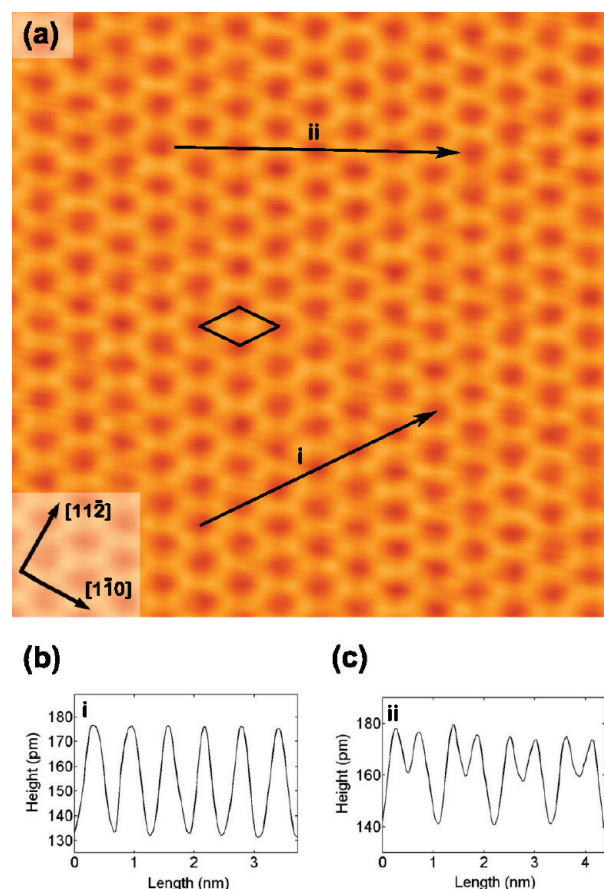

Figure 3. (a) High resolution STM image of the honeycomb structure with bright Ti atoms forming hexagonal rings. A (2 × 2) unit cell is indicated in the image (Image size: 8.5 × 8.5 nm², V_s = 0.98 V, I_t = 0.20 nA). (b),(c) Profiles taken along arrows marked as "i" and "ii" in (a), respectively.

mode which is more sensitive to small atomic corrugations on flat surfaces. All of the other images in this work were obtained while using constant current imaging mode. The periodicities along the spokes and within the triangles share the same measured value of 3.2 ± 0.1 Å.

Triangular TiO_x islands formed by postoxidation annealing in UHV for 1.5 h following 5 ML Ti deposition are shown in Figure 5a. Row-like structures, as shown in Figure 1i, run along the three directions [$\bar{1}$01], [1$\bar{1}$0] and [01$\bar{1}$] of the Au(111) surface. Two line profiles (Figure 5b,c) are drawn along arrows marked as "i" and "ii". Figure 5b shows the measured step height (around 2.3 Å) and the periodicity across the rows (∼8.2 Å). The periodicity along the rows is approximately 3.2 Å, as shown in Figure 5c.

Auger Electron Spectroscopy. Auger spectroscopy was performed on the TiO_x structures on Au(111), and on a rutile $TiO_2(110)$ crystal used as a reference. Although stoichiometric TiO_2 crystals are insulating, they become reduced and electrically conducting, as they change in color from transparent to blue following UHV annealing.[49] To facilitate AES analysis, the TiO_2 reference sample was annealed in UHV to render it conducting enough for AES. The annealed sample has a light blue color. On the basis of comparisons with the literature,[50−52] the sample is estimated to have a composition of TiO_{2-x} ($x < 10^{-4}$). This gives Ti and O Auger peak heights that are close to that of stoichiometric TiO_2. We will refer to this slightly reduced sample
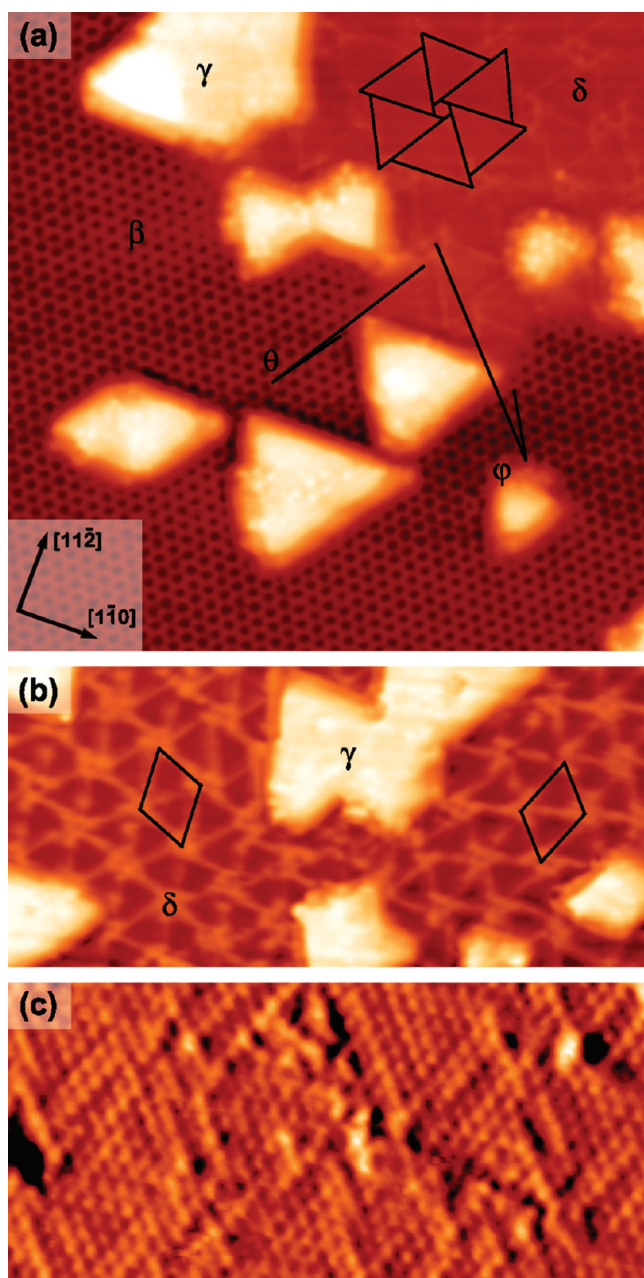
Figure 4. (a) STM image of a TiO_x surface with coexisting honeycomb structure, pinwheel structure, and triangular islands. An asymmetrical pinwheel is drawn with black lines as six triangles. The spoke and the unit cell of the pinwheels are rotated by θ (approximately 2°) and φ (approximately 13°) with respect to the honeycomb structure (Image size: 24 × 24 nm², V_s = 0.98 V, I_t = 0.20 nA). (b) STM image showing two domains of the pinwheel structure (Image size: 31 × 14 nm², V_s = 1.41 V, I_t = 0.18 nA). (c) Constant height atomic resolution image of the pinwheel structure (Image size: 11 × 5 nm², V_s = −0.12 V, I_t = 0.50 nA).

Figure 5. (a) STM image of the row features on the triangular islands (Image size: 23 × 23 nm², V_s = 0.70 V, I_t = 0.29 nA). (b) Measurement along "i" showing the step height (2.3 Å) and the periodicity across the rows (8.2 Å). (c) A line scan along "ii" with a measured periodicity along the rows of 3.2 Å.

as "TiO_2" for simplicity. An Auger spectrum of the TiO_2 reference sample is shown in Figure 6a. The peaks at 380 and 413 eV arise from Ti (LMM & LMV) Auger transitions, while the peaks at 492 and 510 eV are attributed to O (KLL). All of the Auger spectra have a featureless region from 530 to 540 eV that is independent of surface composition. Spectra are normalized by setting the counts at 535 eV to 1000 such that the featureless
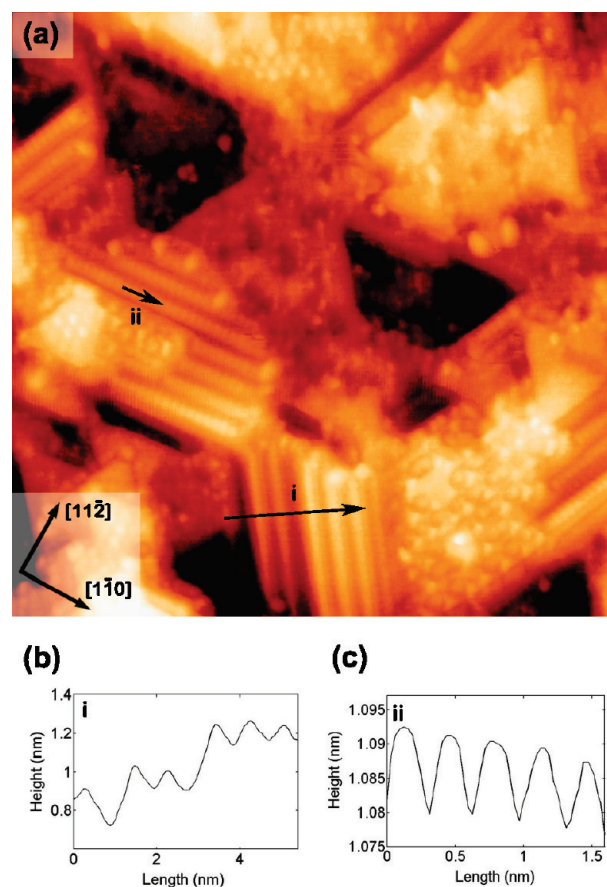
region of each spectrum overlaps. Normalizing the spectra allows for quantitative comparisons of peak heights.

Figure 6b shows the Auger spectrum (solid line) of the surface with multiple TiO_x phases shown in Figure 1d. It has approximate relative surface coverages of honeycomb 80%, triangular islands 10%, and bare reconstructed Au substrate 10%. Since the honeycomb TiO_x structure forms in the submonolayer regime, there is a significant contribution from the Au substrate to the Auger spectrum. Consequently, it is necessary to subtract the Au background signal from the spectrum. An Auger spectrum is shown as a dashed line in Figure 6b which was taken from a clean reconstructed Au surface similar to that shown in Figure 1a. The Au background subtraction results in the difference spectrum shown in Figure 6c. In Figure 6d, an Auger spectrum is shown from a surface covered by triangular islands, formed after 5 MLs Ti deposition similar to the STM image shown in Figure 1i. The spectrum of this thicker film is similar to the stoichiometric TiO_2 sample and as a result background subtraction of the Au substrate is unnecessary.

The chemical composition of the films can be determined by comparing the ratio of related O and Ti peak intensities to that of the TiO_2 crystal. To establish the experimental error of the different TiO_x thin films, five separate Auger spectra were taken for each surface structure from areas approximately 1 mm apart on the same sample. By comparing the O to Ti peak intensity
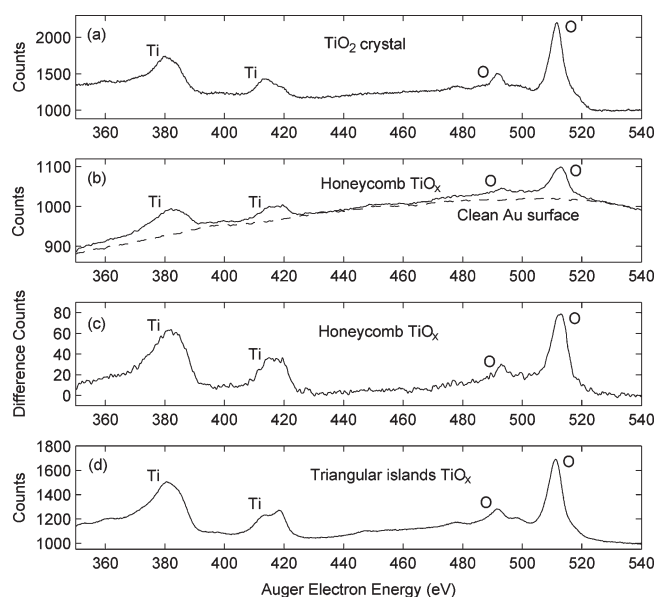
8647

dx.doi.org/10.1021/jp111385n |*J. Phys. Chem. C* 2011, 115, 8643–8652

Figure 6. (a) Auger spectrum of a rutile $TiO_2(110)$ crystal showing the Ti (LMM & LMV) peaks at 380 and 413 eV, and the O (KLL) peaks at 492 and 510 eV. (b) Auger spectrum (solid line) of thin TiO_x film (0.6 MLs) consisting primarily of the honeycomb structure. The dashed line is a spectrum from a clean Au(111) substrate. (c) Difference spectrum showing the subtraction of the Au substrate from the TiO_x thin film spectrum in (b). (d) Auger spectrum of the triangular TiO_x structure formed by 5 MLs of Ti deposition.

Figure 7. Auger spectra showing the Ti $L_3(Ti)M_{23}(Ti)V(O)$ peak at 413 eV, and the Ti $L_3(Ti)M_{23}(Ti)V(Ti)$ peak at 419 eV generated from (a) a slightly reduced rutile TiO_2 surface, (b) a surface covered primarily with the honeycomb structure, and (c) a surface consisting only of triangular islands.

ratios, an average stoichiometry of $TiO_{1.13\pm0.05}$ is calculated for the mixed phase of honeycomb and triangular islands, while for triangular islands, the average stoichiometry is $TiO_{1.30\pm0.04}$. The errors in the stoichiometries are the standard deviations of the combined errors of multiple measurements. For a variety of reasons, outlined below, these stoichiometries require further refinement for them to be accurate.

For ultrathin TiO_x thin films, an important factor to be taken into account is the inelastic electron mean free path (MFP). Auger electrons originated from the O(KLL) and Ti(LMM) transitions have different kinetic energies, and hence different MFPs. Various models for MFP calculation have been proposed in the literature.[53−59] The average MFP based on prevailing models for the Auger electrons in the TiO_2 crystal originating from O(KLL) is 11.32 Å, and for Ti(LMM) is 8.94 Å. This means a relatively larger depth contribution from O than Ti for Auger measurements on the TiO_2 crystal. However, this effect can be ignored for AES on ultrathin TiO_x films on Au, as the depth of the TiO_x layers is less than the MFP. Consequently, it is necessary to use the MFP ratio as a correction factor for the stoichiometry calculation of ultrathin films. The average MFP ratio of the models is 1.25 ± 0.11. The error is the standard deviation of MFP ratios based on different models. By taking the MFP correction factor into account, the corrected stoichiometry is $TiO_{1.41\pm0.19}$ for the honeycomb structure. The error in the corrected stoichiometry is the combined error given by $x\Delta y + y\Delta x + \Delta x\Delta y$, where x and Δx are the average stoichiometry and the standard deviation of multiple measurements; y and Δy are the MFP correction factor and its error. When the surface coverage of the honeycomb structure is considered relative to that of the bare Au surface and the triangular islands in the mixed phase, the stoichiometry of an isolated honeycomb structure is
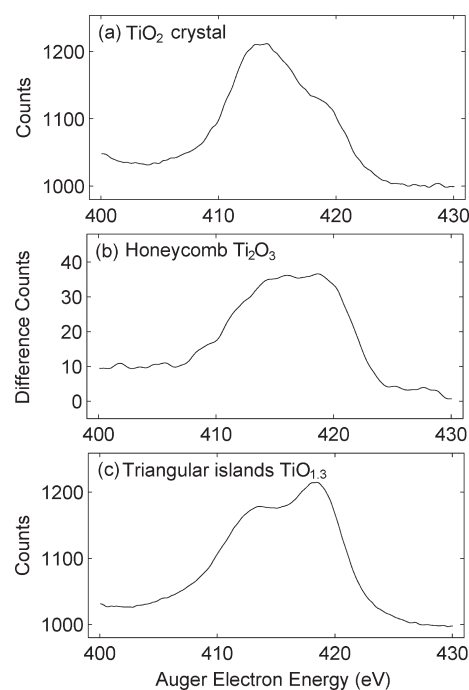
likely to be Ti_2O_3. It was not possible to obtain an isolated Auger spectrum of the pinwheel structure as it always coexists with the honeycomb and the triangular island structures. Limited stoichiometry analysis is available in the literature, among which Schoiswohl et al[39] found that on an O-precovered Rh(111) surface, a pinwheel VO structure could be obtained by depositing the same amount of V as O. The stoichiometry of VO was also supported by density functional theory (DFT) calculations. The pinwheel phase of TiO_x on Au(111) exhibits a similar structure to the pinwheel VO on Rh(111). It is, therefore, possible that they have similar stoichiometries.

The thicker film of the triangular islands shows very small peaks of the Au substrate at the high energy end of the Auger spectrum. The observation of small Au peaks is due to the large MFP (∼25.87 Å) of the Auger electrons generated from the Au substrate. Consequently, for Ti and O peaks originated from much smaller MFPs, the thicker film can be considered as a bulk sample for Auger purposes and no MFP correction is necessary for the stoichiometry calculation of $TiO_{1.30\pm0.04}$. It should be noted, however, that effects such as shadowing and Auger electron diffraction will further contribute to the error on the stoichiometry by as much as 10%.

Figure 7 shows high resolution Auger spectra of the Ti peak at 413 eV for stoichiometric TiO_2, the honeycomb (2×2) surface and a surface consisting of triangular islands. Each of these spectra have significant differences in their peak shapes. The TiO_2 spectrum in Figure 7a consists of a peak at 413 eV with a shoulder at 419 eV, while for the triangular islands (Figure 7c), a distinct peak at 419 eV is visible with the 413 eV peak appearing as a shoulder. In Figure 7b, the peak for the honeycomb structure appears flat, which can be attributed to the peaks at 413 and 419 eV

having equal heights. Previous studies[60−68] on titanium oxides indicate that the structure of the peak at 400−430 eV is sensitive to Ti oxidation states. The two components of the peak at 413 and 419 eV are thought to arise from inter- and intra-atomic transitions connected with the valence band.[61,62,65] The peak at 413 eV is attributed to the $L_3(Ti)M_{23}(Ti)V(O)$ interatomic transitions involving the oxygen 2p level, while the peak at 419 eV originates from the $L_3(Ti)M_{23}(Ti)V(Ti)$ intra-atomic transitions involving the titanium 3d level. For Ti metal, only the peak at 419 eV has been observed in Auger spectra[62,64] as the $L_3(Ti)M_{23}(Ti)V(O)$ Auger transitions cannot occur without oxygen ions. As for stoichiometric TiO_2, ideally there would only be the peak at 413 eV[60,65] since the Ti 3d level is vacant. The measured Auger spectra, however, usually have a shoulder at 419 eV (Figure 7a) due to the presence of Ti 3d electrons that arise as a result of a small number of oxygen vacancies introduced during UHV annealing. The intensity of the 413 eV peak is proportional to the amount of oxygen in the surface region, and the 419 eV peak is a measure of the 3d electron density. Hence, one peak wanes as the other waxes in accordance with the different oxidation states.

The Auger peak shape in Figure 7 is consistent with the stoichiometries determined by the peak intensities, indicating a higher oxidation state for the honeycomb structure with a stoichiometry around Ti_2O_3 compared to the triangular island structure with a stoichiometry of approximately $TiO_{1.3}$. It should be pointed out that charge transfer from the Ti 3d level to the Au substrate can affect the Ti(LMV) peak of the ultrathin TiO_x film. The effect has been reported for Au nanoclusters grown on reduced $TiO_2(110)$[69−73] and TiO_2-terminated $SrTiO_3(001)$ substrates,[74] where electronic charge transfers from the valence band of the supporting oxides to Au at the interfaces. The resultant electron depletion of the Ti 3d level leads to a reduction in the number of $L_3(Ti)M_{23}(Ti)V(Ti)$ Auger transitions for the honeycomb structure in the monolayer regime. As this charge transfer only occurs at the interface, Auger transitions of the thicker film (5 MLs) of triangular islands are not affected. Interestingly, exposure of the samples to air fully oxidizes the substoichiometric TiO_x thin films. This can be observed as a higher O to Ti peak intensity ratio and Ti peak (413 eV) shape similar to that of TiO_2 in the Auger spectra. The substoichiometric oxidation states, however, are restored following UHV annealing to the growth temperature of the thin films (600 °C).

Structural Models. On the basis of the STM images and AES spectra, an atomic model is shown in Figure 8, for the (2×2)-reconstructed honeycomb structure. Ti atoms (blue balls) occupy 3-fold hollow sites of the Au lattice (yellow balls). For each Ti atom, the three nearest neighbor and six next nearest neighbor hollow sites are vacant, and the third nearest neighbor sites are occupied. These occupation rules result in the hexagonal lattice show in Figure 8a. The model is based on STM images (e.g., Figure 3a), which show that six Ti atoms (bright) form a hexagon with a hole in the center. The centers of the hexagons formed by the Ti atoms form the corners of the (2×2) unit cell drawn in Figure 8. The Ti layer can also be viewed as a hexagonal lattice with the interatomic spacing of 3.33 Å rotated by 30° with respect to the Au lattice. The density of Ti atoms is 0.50 per (1×1) Au surface unit cell. The oxygen atoms (red balls) are located at the bridging sites of the Ti atoms (Figure 8b), resulting in Ti_2O_3 stoichiometry, which matches the AES data. This model is substantially the same as previously proposed for honeycomb TiO_x structures.[15,38]
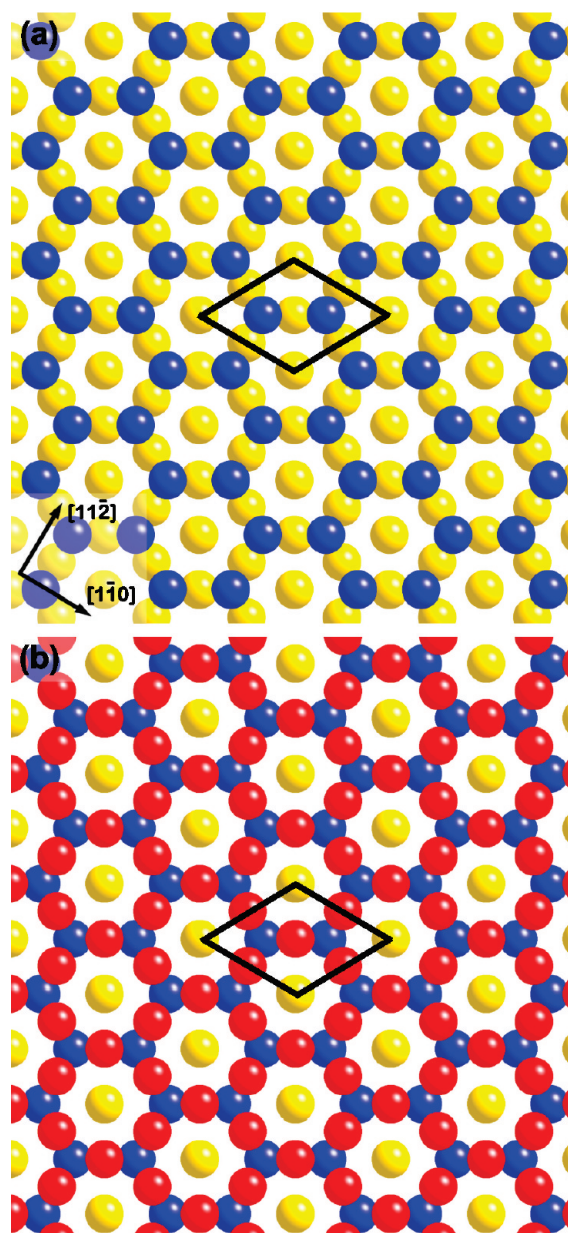

Figure 8. (a) An atomic model for the hexagonal honeycomb structure with Ti atoms sitting in 3-fold hollow sites of the Au(111) substrate. Au atoms are yellow while Ti atoms are blue. (b) Same model with oxygen atoms (red) located at the bridging sites of the Ti atoms. The (2×2) unit cell is indicated on both images.

For the pinwheel structure, the STM images in Figure 4 can be explained by a Moiré pattern formed by superpositioning a Ti lattice over the Au(111)-(1×1) surface as shown in Figure 9. The condition of coincident points for two lattices can be calculated using the following equation:[75,76]

$$\begin{pmatrix} s & \frac{1}{2}s \\ 0 & \frac{\sqrt{3}}{2}s \end{pmatrix} \begin{pmatrix} h \\ k \end{pmatrix} = \begin{pmatrix} \cos\theta & -\sin\theta \\ \sin\theta & \cos\theta \end{pmatrix} \begin{pmatrix} a & \frac{1}{2}a \\ 0 & \frac{\sqrt{3}}{2}a \end{pmatrix} \begin{pmatrix} m \\ n \end{pmatrix} \quad (1)$$

where s and a are the atomic spacings of the Au substrate layer and the Ti adlayer, respectively; θ is the angle between the two

8649

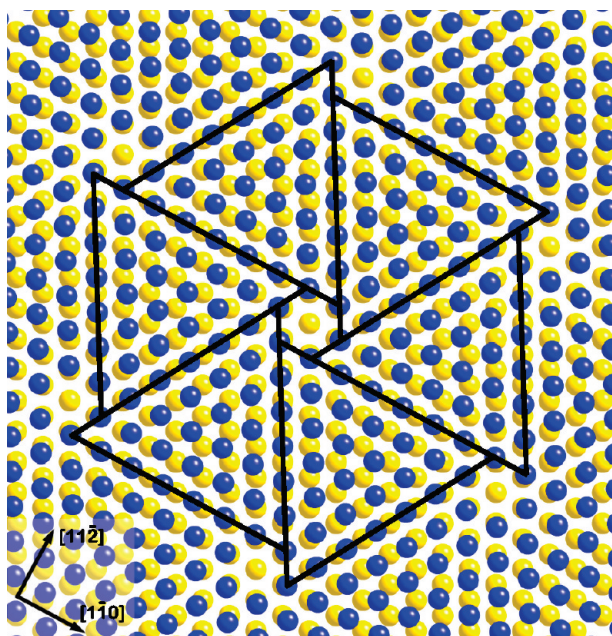dx.doi.org/10.1021/jp111385n |*J. Phys. Chem. C* 2011, 115, 8643–8652

Figure 9. Model for the pinwheel structure where Ti atoms are arranged in a rotated lattice (blue, 3.27 Å periodicity) on the Au(111) surface (yellow, 2.89 Å periodicity). The position of the oxygen atoms is not shown. The six triangles that make up the pinwheel are drawn on the image. The Moiré pattern that results can be described as a $(\sqrt{67} \times \sqrt{67})R12.2°$ reconstruction.

layers; h, k, and m, n are integer multiples resulting in the coincidence between the lattices. Equation 1 can be solved for the variables a and θ such that:

$$a = s\sqrt{\frac{h^2 + hk + k^2}{m^2 + mn + n^2}};$$

$$\theta = \arctan\left(\frac{\sqrt{3}(km - hn)}{2hm + hn + km + 2kn}\right) \quad (2)$$

From eq 1, the coincidence periodicity r (Moiré periodicity) and angle φ between the Moiré pattern and the substrate can also be determined:

$$r = \frac{s}{2}\sqrt{(2h + k)^2 + 3k^2}; \quad \varphi = \arctan\left(\frac{\sqrt{3}k}{2h + k}\right) \quad (3)$$

With s fixed at 2.89 Å, eq 3 was used to determine candidate integer multiples h and k based on the ranges of r and φ measured from STM images. The candidate compatible pairs were substituted into eq 2 to calculate possible sets of integer m and n which fit the measured range of a and θ. The compatible sets of integer h, k, m, and n were then considered for further analysis. A Moiré pattern which matches the STM images can be reproduced with the parametres $h = 7$, $k = 2$, $m = 2$, $n = 9$, $s = 2.89$ Å, $\theta = 1.68°$, and $a = 3.27$ Å. On the basis of these calculations, we propose an atomic model for the pinwheel structure shown in Figure 9 with a Ti adlayer (3.27 Å periodicity) rotated anti-clockwise by 1.68° with respect to the Au(111) lattice (2.89 Å periodicity) underneath. The other domain can be obtained by rotating the Ti lattice clockwise instead. A pinwheel is drawn on the model. In Figure 9, the Ti atoms at the triangle edges are located

at Au bridging sites. Consequently, they appear brighter than the other Ti atoms in the STM images (Figure 4). This model produces a $(\sqrt{67} \times \sqrt{67})R12.2°$ reconstruction. The density of Ti atoms is 0.76 per (1×1) Au unit cell. For the VO pinwheel structure on Rh(111), a model was proposed based on DFT calculations.[39] It contains a V hexagonal layer with O atoms occupying the 3-fold hollow sites on top. For the pinwheel TiO_x structure on Au(111), O atoms are likely to be stable at the hollow sites or the bridging sites of the Ti layer underneath. A TiO stoichiometry results from both possibilities, although theoretical studies would be useful to locate the O position in this model.

We have so far proposed atomic structures for the monolayer honeycomb and pinwheel surfaces. The third structure, namely the triangular islands, is thicker and consists of multiple layers. STM imaging and Auger spectroscopy data alone are not sufficient in this instance to allow us to propose a structural model. However, we can rule out that the triangular islands are a TiO_2 polymorph because our Auger data indicates a stoichiometry of $TiO_{1.30\pm0.04}$.

■ DISCUSSION

It is instructive to compare the proposed ultrathin TiO_x film structures with those grown on other substrates. Comparable honeycomb TiO_x structures similar to those presented here were studied by other researchers on metal substrates such as Ru-(0001), Cu(001), and Pt(111). On Cu(001)[25] and Ru(0001),[11] an O—Ti—O trilayer structure was proposed for both honeycomb TiO_x structures observed. Whether a stacking type of O—Ti—metal or Ti—O—metal is preferable depends strongly on the substrate used. Au is nobler than Ru, Cu, and even Pt, and is very unlikely to bond with O. Instead, it has been reported that for Au deposited on reduced TiO_2, Au is trapped at the oxygen vacancies and binds to the substrate via Ti incorporating a charge transfer mechanism.[70−72,77] Hence, for our system the O—Ti—Au stacking sequence is likely to be energetically favorable compared with Ti—O—Au stacking. For TiO_x grown on Pt-(111), Sedona et al. have reported STM observations similar to those shown here and proposed a model with Ti atoms sitting at Pt(111) hollow sites and O atoms at Ti bridging sites.[15,38] XPS indicated stacking of Pt—Ti—O. The proposed model was later modeled by DFT calculations[38] and has a stoichiometry of Ti_2O_3. A similar model has also been proposed for a V_2O_3 structure on Pd(111).[78−80] Our AES data in Figure 6 confirm that the honeycomb structure on Au(111) has a stoichiometry of Ti_2O_3. Combined STM and AES data indicate that the honeycomb Ti_2O_3 phase on Au(111) has a similar structure to the Ti_2O_3 phase on Pt(111) and the V_2O_3 phase on Pd(111).

Similar pinwheel or wagon-wheel-like phases as presented here have been found in other systems, such as encapsulated TiO_x on Pd(111) nanoparticles on $TiO_2(110)$[36,81] and TiO_x/Pt(111).[15,17,18,38] The TiO_x wagon-wheel structures are usually attributed to Moiré-like models. There has, however, been disagreement on the stacking sequence. Compared to the O—Ti—metal stacking with the formation of a Moiré pattern between Ti and substrate lattices, STM observations can also be explained by superpositioning a Ti layer on an O layer which adopts the substrate lattice, and this results in Ti—O—metal stacking. Our model adopts O—Ti—Au stacking for the pinwheel structure, since the Au substrate is likely to bind with Ti due to charge transfer. This energetically favorable O—Ti—Au stacking sequence also restricts the possibility of the growth of other structures directly on Au. In the monolayer regime, the

honeycomb and the pinwheel TiO_x are the only two structures observed on Au(111). On metal substrates such as Pt(111) and Pd(111), other phases, namely the zigzag structures, were also observed at submonolayer coverages.[15,36] Both models proposed for the zigzag structures involve oxygen atoms at the interfaces. As it is unlikely for O to form an epitaxial layer on Au as may occur on Pd and Pt, no zigzag structure forms on Au and only honeycomb and pinwheel phases were observed in the monolayer regime. The pinwheel structure coexists with the honeycomb structure, especially around 1 ML coverage. What seems plausible is that the honeycomb structure has a lower surface energy compared with the pinwheel structure, but that the pinwheel structure is adopted in order to accommodate the increased density of deposited Ti. After all, the pinwheel structure is more than 1.5 times as dense as the honeycomb. This proposal is further supported by the observation that the pinwheel structure transforms into the honeycomb structure upon UHV annealing at 600 °C.

Triangular TiO_2 islands have recently been reported on Au-(111) by Potapenko et al. using Ti—Au alloy oxidation,[35] however the structure of the triangles was not resolved. A hexagonal shape was reported to coexist with the triangular shape. In their previous study on preparing TiO_2 nanocrystals on Au(111) by reactive-layer-assisted deposition, a row structure was observed on hexagonal crystallites.[34] The spacing across the rows and the height of the hexagonal islands have been measured to be 9.0—9.5 Å and 2.3 Å, respectively. The authors proposed a (1×2) reconstruction on the rutile $TiO_2(100)$ surface. Our STM measurements of the row structure on the triangular TiO_x islands suggests similar heights of the triangular islands (~2.3 Å) but a slightly smaller periodicity (8.2 Å). We do not have sufficient data to speculate on the structure of our triangular island covered surfaces except to state that given our Auger data indicating $TiO_{1.3}$ stoichiometry, we do not think that these are bulk terminations of a TiO_2 polymorph.

■ CONCLUSIONS

In summary, TiO_x thin films were grown on the herringbone-reconstructed Au(111) surface following Ti deposition and oxidation. As the Ti coverage was increased, we observed three distinct structures: honeycombs, pinwheels, and triangular islands. With Ti coverages of less than 0.5 ML, the Ti atoms occupy the third nearest neighbor hollow sites of the Au(111) lattice, forming the (2×2) honeycomb Ti_2O_3 structure. To accommodate more Ti atoms, a closer packed structure with a pinwheel shape arises. This structure is seen for Ti deposition from 0.5 to 1.8 MLs. The $(\sqrt{67} \times \sqrt{67})R12.2°$ reconstructed pinwheel structure has a higher Ti density and can be described as a Moiré pattern. Further increasing the Ti coverage results in the formation of $TiO_{1.3}$ multiple layers with a characteristic triangular shape.

Besides TiO_x thin films grown on different metal substrates, similar honeycomb and pinwheel structures have been observed[37,39,78−80,82−84] for oxides of other transition metals with multiple oxidation states, such as VO_x and FeO_x. Such studies open up a new research area in which novel structures can be created and utilized in a variety of applications. Similarly, the TiO_x structures on Au(111) reported here were not observed on bulk TiO_2 terminations and they potentially have different properties relevant to catalysts, gas sensors, and solar cells. Well-ordered epitaxial TiO_x thin film structures on Au(111) presented in this work also serve as promising templates for the growth of metal clusters, particularly for

catalytically relevant Au nanoparticles.[85−88] The study of thin oxide films on noble metals provides insights into fundamental oxide-metal interactions at the interface. This is of significant importance for the investigation of catalytic properties of oxides, and oxide-supported noble metal nanoparticles.

■ AUTHOR INFORMATION

Corresponding Author
*Phone: +44 (0)1865 273770. Fax: +44 (0)1865 273783. E-mail: chen.wu@materials.ox.ac.uk; martin.castell@materials.ox.ac.uk.

Present Addresses
‡Department of Applied Physics and CRISP, Yale University, New Haven, Connecticut 06520, United States

■ REFERENCES

(1) Yu, J. G.; Zhao, X. J.; Zhao, Q. N. *Thin Solid Films* **2000**, *379*, 7–14.

(2) Anpo, M.; Takeuchi, M. *J. Catal.* **2003**, *216*, 505–516.

(3) Diebold, U. *Surf. Sci. Rep.* **2003**, *48*, 53–229.

(4) Enache, D. I.; Edwards, J. K.; Landon, P.; Solsona-Espriu, B.; Carley, A. F.; Herzing, A. A.; Watanabe, M.; Kiely, C. J.; Knight, D. W.; Hutchings, G. J. *Science* **2006**, *311*, 362–365.

(5) Ruiz, A. M.; Sakai, G.; Cornet, A.; Shimanoe, K.; Morante, J. R.; Yamazoe, N. *Sens. Actuators, B* **2003**, *93*, 509–518.

(6) Serra, A.; Filippo, E.; Buccolieri, A.; Di Giulio, M.; Manno, D. *Sens. Actuators, B* **2009**, *140*, 563–567.

(7) Mohammadi, M. R.; Fray, D. J. *Sens. Actuators, B* **2009**, *141*, 76–84.

(8) Kiema, G. K.; Colgan, M. J.; Brett, M. J. *Sol. Energy Mater. Sol. Cells* **2005**, *85*, 321–331.

(9) Zhang, Y.; Xie, Z. B.; Wang, J. *ACS Appl. Mater. Interfaces* **2009**, *1*, 2789–2795.

(10) Kim, Y.; Kim, C. H.; Lee, Y.; Kim, K. J. *Chem. Mater.* **2010**, *22*, 207–211.

(11) Mannig, A.; Zhao, Z.; Rosenthal, D.; Christmann, K.; Hoster, H.; Rauscher, H.; Behm, R. J. *Surf. Sci.* **2005**, *576*, 29–44.

(12) Ashworth, T. V.; Thornton, G. *Thin Solid Films* **2001**, *400*, 43–45.

(13) Papageorgiou, A. C.; Pang, C. L.; Chen, Q.; Thornton, G. *ACS Nano* **2007**, *1*, 409–414.

(14) Papageorgiou, A. C.; Cabailh, G.; Chen, Q.; Resta, A.; Lundgren, E.; Andersen, J. N.; Thornton, G. *J. Phys. Chem. C* **2007**, *111*, 7704–7710.

(15) Sedona, F.; Rizzi, G. A.; Agnoli, S.; Llabres i Xamena, F. X.; Papageorgiou, A.; Ostermann, D.; Sambi, M.; Finetti, P.; Schierbaum, K.; Granozzi, G. *J. Phys. Chem. B* **2005**, *109*, 24411–24426.

(16) Sedona, F.; Eusebio, M.; Rizzi, G. A.; Granozzi, G.; Ostermann, D.; Schierbaum, K. *Phys. Chem. Chem. Phys.* **2005**, *7*, 697–702.

(17) Sedona, F.; Agnoli, S.; Granozzi, G. *J. Phys. Chem. B* **2006**, *110*, 15359–15367.

(18) Finetti, P.; Sedona, F.; Rizzi, G. A.; Mick, U.; Sutara, F.; Svec, M.; Matolin, V.; Schierbaum, K.; Granozzi, G. *J. Phys. Chem. C* **2007**, *111*, 869–876.

(19) Barcaro, G.; Agnoli, S.; Sedona, F.; Rizzi, G. A.; Fortunelli, A.; Granozzi, G. *J. Phys. Chem. C* **2007**, *111*, 6095–6102.

8651

dx.doi.org/10.1021/jp111385n |*J. Phys. Chem. C* 2011, 115, 8643–8652

(20) Sedona, F.; Granozzi, G.; Barcaro, G.; Fortunelli, A. *Phys. Rev. B* **2008**, *77*, 115417.

(21) Matsumoto, T.; Batzill, M.; Hsien, S.; Koel, B. E. *Surf. Sci.* **2004**, *572*, 127–145.

(22) Matsumoto, T.; Batzill, M.; Hsien, S.; Koel, B. E. *Surf. Sci.* **2004**, *572*, 146–161.

(23) Chen, M. S.; Wallace, W. T.; Kumar, D.; Yan, Z.; Gath, K. K.; Cai, Y.; Kuroda, Y.; Goodman, D. W. *Surf. Sci.* **2005**, *581*, L115–L121.

(24) Kumar, D.; Chen, M. S.; Goodman, D. W. *Thin Solid Films* **2006**, *515*, 1475–1479.

(25) Maeda, T.; Kobayashi, Y.; Kishi, K. *Surf. Sci.* **1999**, *436*, 249–258.

(26) Finetti, P.; Caffio, M.; Cortigiani, B.; Atrei, A.; Rovida, G. *Surf. Sci.* **2008**, *602*, 1101–1113.

(27) Dulub, O.; Hebenstreit, W.; Diebold, U. *Phys. Rev. Lett.* **2000**, *84*, 3646–3649.

(28) Jennison, D. R.; Dulub, O.; Hebenstreit, W.; Diebold, U. *Surf. Sci.* **2001**, *492*, L677–L687.

(29) Tauster, S. J.; Fung, S. C.; Garten, R. L. *J. Am. Chem. Soc.* **1978**, *100*, 170–175.

(30) Ando, M.; Kobayashi, T.; Haruta, M. *Catal. Today* **1997**, *36*, 135–141.

(31) Chen, M. S.; Goodman, D. W. *Science* **2004**, *306*, 252–255.

(32) Biener, J.; Farfan-Arribas, E.; Biener, M.; Friend, C. M.; Madix, R. J. *J. Chem. Phys.* **2005**, *123*, 094705.

(33) Song, D.; Hrbek, J.; Osgood, R. *Nano Lett.* **2005**, *5*, 1327–1332.

(34) Potapenko, D. V.; Hrbek, J.; Osgood, R. M. *ACS Nano* **2008**, *2*, 1353–1362.

(35) Potapenko, D. V.; Osgood, R. M. *Nano Lett.* **2009**, *9*, 2378–2383.

(36) Bennett, R. A.; Pang, C. L.; Perkins, N.; Smith, R. D.; Morrall, P.; Kvon, R. I.; Bowker, M. *J. Phys. Chem. B* **2002**, *106*, 4688–4696.

(37) Surnev, S.; Vitali, L.; Ramsey, M. G.; Netzer, F. P.; Kresse, G.; Hafner, J. *Phys. Rev. B* **2000**, *61*, 13945–13954.

(38) Barcaro, G.; Agnoli, S.; Sedona, F.; Rizzi, G. A.; Fortunelli, A.; Granozzi, G. *J. Phys. Chem. C* **2009**, *113*, 5721–5729.

(39) Schoiswohl, J.; Surnev, S.; Stock, M.; Eck, S.; Ramsey, M. G.; Netzer, F. P. *Phys. Rev. B* **2005**, *71*, 165437.

(40) Horcas, I.; Fernandez, R.; Gomez-Rodriquez, J. M.; Colchero, J.; Gomez-Herrero, J.; Baro, A. M. *Rev. Sci. Instrum.* **2007**, *78*, 013705.

(41) Silly, F. *J. Microsc.* **2009**, *236*, 211–218.

(42) Barth, J. V.; Brune, H.; Ertl, G.; Behm, R. J. *Phys. Rev. B* **1990**, *42*, 9307–9318.

(43) Silly, F.; Shaw, A. Q.; Briggs, G. A. D.; Castell, M. R. *Appl. Phys. Lett.* **2008**, *92*, 023102.

(44) Diebold, U.; Anderson, J. F.; Ng, K. O.; Vanderbilt, D. *Phys. Rev. Lett.* **1996**, *77*, 1322–1325.

(45) Yagi, E.; Hasiguti, R. R.; Aono, M. *Phys. Rev. B* **1996**, *54*, 7945–7956.

(46) Silly, F.; Castell, M. R. *Phys. Rev. Lett.* **2006**, *96*, 086104.

(47) Guo, Q.; Cocks, I.; Williams, E. M. *J. Phys. D: Appl. Phys.* **1998**, *31*, 2231–2235.

(48) Calleja, F.; Arnau, A.; Hinarejos, J. J.; de Parga, A. L. V.; Hofer, W. A.; Echenique, P. M.; Miranda, R. *Phys. Rev. Lett.* **2004**, *92*, 206101.

(49) Li, M.; Hebenstreit, W.; Diebold, U.; Tyryshkin, A. M.; Bowman, M. K.; Dunham, G. G.; Henderson, M. A. *J. Phys. Chem. B* **2000**, *104*, 4944–4950.

(50) Bennett, R. A.; Poulston, S.; Stone, P.; Bowker, M. *Phys. Rev. B* **1999**, *59*, 10341–10346.

(51) Bennett, R. A.; Stone, P.; Price, N. J.; Bowker, M. *Phys. Rev. Lett.* **1999**, *82*, 3831–3834.

(52) Bowker, M.; Bennett, R. A. *J. Phys.: Condens. Matter* **2009**, *47*, 474224.

(53) Seah, M. P. *Surf. Interface Anal.* **1986**, *9*, 85–98.

(54) Penn, D. R. *J. Electron Spectrosc. Relat. Phenom.* **1976**, *9*, 29–40.

(55) Ashley, J. C. *J. Electron Spectrosc. Relat. Phenom.* **1982**, *28*, 177–194.

(56) Sazajman, J.; Liesegang, J.; Jenkin, J. G.; Leckey, R. C. G. *J. Electron Spectrosc. Relat. Phenom.* **1981**, *23*, 97–102.

(57) Tokutaka, H.; Nishimori, K.; Hayashi, H. *Surf. Sci.* **1985**, *149*, 349–365.

(58) Tanuma, S.; Powell, C. J.; Penn, D. R. *Surf. Interface Anal.* **1994**, *21*, 165–176.

(59) Seah, M. P.; Dench, W. A. *Surf. Interface Anal.* **1979**, *1*, 2–11.

(60) Solomon, J. S.; Baun, W. L. *Surf. Sci.* **1975**, *51*, 228–236.

(61) Rao, C. N. R.; Sarma, D. D. *Phys. Rev. B* **1982**, *25*, 2927–2929.

(62) Nishigaki, S. *Surf. Sci.* **1983**, *125*, 762–770.

(63) Davis, G. D.; Natan, M.; Anderson, K. A. *Appl. Surf. Sci.* **1983**, *15*, 321–333.

(64) Roman, E.; Sanchez-Avedillo, M.; de Segovia, J. L. *Appl. Phys. A: Mater. Sci. Process.* **1984**, *35*, 35–40.

(65) Gopel, W.; Anderson, J. A.; Frankel, D.; Jaehnig, M.; Phillips, K.; Schafer, J. A.; Rocker, G. *Surf. Sci.* **1984**, *139*, 333–346.

(66) Vaquila, I.; Passeggi, M. C. G.; Ferron, J. *Phys. Rev. B* **1997**, *55*, 13925–13931.

(67) Vaquila, I.; Vergara, L. I.; Passeggi, M. C. G.; Vidal, R. A.; Ferron, J. *Surf. Coat. Technol.* **1999**, *122*, 67–71.

(68) Brasca, R.; Vergara, L.; Passeggi, M. C. G.; Ferróna, J. *Mat. Res.* **2007**, *10*, 283–288.

(69) Howard, A.; Clark, D. N. S.; Mitchell, C. E. J.; Egdell, R. G.; Dhanak, V. R. *Surf. Sci.* **2002**, *518*, 210–224.

(70) Vijay, A.; Mills, G.; Metiu, H. *J. Chem. Phys.* **2003**, *118*, 6536–6551.

(71) Worz, A. S.; Heiz, U.; Cinquini, F.; Pacchioni, G. *J. Phys. Chem. B* **2005**, *109*, 18418–18426.

(72) Chen, M.; Goodman, D. W. *Acc. Chem. Res.* **2006**, *39*, 739–746.

(73) Jiang, Z.; Zhang, W.; Jin, L.; Yang, X.; Xu, F.; Zhu, J.; Huang, W. *J. Phys. Chem. C* **2007**, *111*, 12434–12439.

(74) Mitsuhara, K.; Kitsudo, Y.; Matsumoto, H.; Visikovskiy, A.; Takizawa, M.; Nishimura, T.; Akita, T.; Kido, Y. *Surf. Sci.* **2010**, *604*, 548–554.

(75) Hommrich, J.; Humann, S.; Wandelt, K. *Faraday Discuss.* **2002**, *121*, 129–138.

(76) Silly, F.; Castell, M. R. *J. Phys. Chem. B* **2005**, *109*, 12316–12319.

(77) Vittadini, A.; Selloni, A. *J. Chem. Phys.* **2002**, *117*, 353–361.

(78) Klein, C.; Kresse, G.; Surnev, S.; Netzer, F. P.; Schmid, M.; Varga, P. *Phys. Rev. B* **2003**, *68*, 235416–235426.

(79) Surnev, S.; Kresse, G.; Sock, M.; Ramsey, M. G.; Netzer, F. P. *Surf. Sci.* **2001**, *459*, 91–106.

(80) Sambi, M.; Petukhov, M.; Domenichini, B.; Rizzi, G. A.; Surnev, S.; Kresse, G.; Netzer, F. P.; Granozzi, G. *Surf. Sci.* **2003**, *529*, L234–L238.

(81) Bowker, M.; Stone, P.; Morrall, P.; Smith, R.; Bennet, R.; Perkins, N.; Kvon, R.; Pang, C.; Fourre, E.; Hall, M. *J. Catal.* **2005**, *234*, 172–181.

(82) Schoiswohl, J.; Surnev, S.; Stock, M.; Eck, S.; Ramsey, M. G.; Netzer, F. P.; Kresse, G. *Phys. Rev. B* **2004**, *69*, 1555403.

(83) Ritter, M.; Ranke, W.; Weiss, W. *Phys. Rev. B* **1998**, *57*, 7240–7251.

(84) Weiss, W.; Ranke, W. *Prog. Surf. Sci.* **2002**, *70*, 1–151.

(85) Sedona, F.; Agnoli, S.; Fanetti, M.; Kholmanov, I.; Cavaliere, E.; Gavioli, L.; Granozzi, G. *J. Phys. Chem. C* **2007**, *111*, 8024–8029.

(86) Rizzi, G. A.; Sedona, F.; Artiglia, L.; Agnoli, S.; Barcaro, G.; Fortunelli, A.; Cavaliere, E.; Gavioli, L.; Granozzi, G. *Phys. Chem. Chem. Phys.* **2009**, *11*, 2177–2185.

(87) Barcaro, G.; Fortunelli, A.; Granozzi, G.; Sedona, F. *J. Phys. Chem. C* **2009**, *113*, 1143–1146.

(88) Cavaliere, E.; Kholmanov, I.; Gavioli, L.; Sedona, F.; Agnoli, S.; Granozzi, G.; Barcaro, G.; Fortunelli, A. *Phys. Chem. Chem. Phys.* **2009**, *11*, 11305–11309.

8652

dx.doi.org/10.1021/jp111385n |*J. Phys. Chem. C* 2011, 115, 8643–8652